Impaired cell growth under ammonium stress explained by modeling the energy cost of vacuole expansion in tomato leaves

Théo Poucet, Bertrand Beauvoit, María Begoña González-Moro, Cecile Cabasson, Pierre Pétriacq, Amélie Flandin, Yves Gibon, Daniel Marino, Martine Dieuaide-Noubhani

HAL Id: hal-03855200
https://hal.inrae.fr/hal-03855200v1

Impaired cell growth under ammonium stress explained by modeling the energy cost of vacuole expansion in tomato leaves

Théo Poucet[1,2] , Bertrand Beauvoit[2,*] , María Begoña González-Moro[1] , Cécile Cabasson[2,3] , Pierre Pétriacq[2,3] [ID],
Amélie Flandin[2,3] , Yves Gibon[2,3] , Daniel Marino[1,4,*,†] and Martine Dieuaide-Noubhani[2,*,†] [ID]

[1]*Department of Plant Biology and Ecology, University of the Basque Country (UPV/EHU), E-48940, Leioa, Spain,*
[2]*Université de Bordeaux, INRAE, UMR Biologie du Fruit et Pathologie, Villenave d'Ornon 33140, France,*
[3]*Bordeaux Metabolome, MetaboHUB, PHENOME-EMPHASIS, Villenave d'Ornon 33140, France, and*
[4]*Ikerbasque, Basque Foundation for Science, E-48011, Bilbao, Spain*

SUMMARY

Ammonium (NH_4^+)-based fertilization efficiently mitigates the adverse effects of nitrogen fertilization on the environment. However, high concentrations of soil NH_4^+ provoke growth inhibition, partly caused by the reduction of cell enlargement and associated with modifications of cell composition, such as an increase of sugars and a decrease in organic acids. Cell expansion depends largely on the osmotic-driven enlargement of the vacuole. However, the involvement of subcellular compartmentation in the adaptation of plants to ammonium nutrition has received little attention, until now. To investigate this, tomato (*Solanum lycopersicum*) plants were cultivated under nitrate and ammonium nutrition and the fourth leaf was harvested at seven developmental stages. The vacuolar expansion was monitored and metabolites and inorganic ion contents, together with intracellular pH, were determined. A data-constrained model was constructed to estimate subcellular concentrations of major metabolites and ions. It was first validated at the three latter developmental stages by comparison with subcellular concentrations obtained experimentally using non-aqueous fractionation. Then, the model was used to estimate the subcellular concentrations at the seven developmental stages and the net vacuolar uptake of solutes along the developmental series. Our results showed ammonium nutrition provokes an acidification of the vacuole and a reduction in the flux of solutes into the vacuoles. Overall, analysis of the subcellular compartmentation reveals a mechanism behind leaf growth inhibition under ammonium stress linked to the higher energy cost of vacuole expansion, as a result of alterations in pH, the inhibition of glycolysis routes and the depletion of organic acids.

Keywords: nitrogen, vacuole expansion, metabolism, pH, *Solanum lycopersicum*, transporter, flux, modeling.

INTRODUCTION

Plants take up nitrogen (N) from the soil, mainly in the form of nitrate (NO_3^-) and ammonium (NH_4^+). Owing to its oxidative state, amino acid synthesis directly from NH_4^+ is energetically more efficient, as the two reductive steps to transform NO_3^- into NH_4^+ are detoured (Hase et al., 2006). Paradoxically, ammonium nutrition can entail a stressful situation that induces a set of symptoms such as chlorosis and biomass reduction (Britto & Kronzucker, 2002). The causes of these symptoms include external cell medium acidification, depleted uptake of inorganic cations through direct competition with the NH_4^+ uptake or the disruption

of hormone balance (Britto & Kronzucker, 2002; Liu & Von Wirén, 2017). In parallel, under severe ammonium stress, the occurrence of oxidative stress has also been associated with the lower reductive power needed for NH_4^+ assimilation (Podgórska et al., 2013). It is known that ammonium syndrome is not caused by a single mechanism alone but rather by a combination of the above-mentioned factors. Although ammonium stress is considered universal, there is high interspecific and intraspecific variability (Cruz et al., 2011; Sarasketa et al., 2014), with some species even displaying a preference for ammonium. For example, among crops, rice (*Oryza sativa*) is considered highly

tolerant to ammonium nutrition (Estebana et al., 2016). In all cases, the genetic basis of this natural variation remains to be discovered.

Walch-Liu et al. (2000) observed that cell number and size were lower in leaves of tobacco (*Nicotiana tabacum*) plants fed with NH_4^+ compared with those fed with NO_3^-, suggesting that cell division and elongation were affected by ammonium nutrition in relation to lower cytokinin levels. Later, a similar impact of NH_4^+ nutrition on Arabidopsis root cells was reported (Liu et al., 2013; Ötvös et al., 2021). Smaller leaf cell size under ammonium nutrition has been associated with higher cell wall stiffness, potentially reducing cell elongation (Podgórska et al., 2017). However, cell expansion also relies on the internal pressure exerted on the cell wall by the vacuole (Kaiser et al., 2021; Kaiser & Scheuring, 2020). Indeed, cell turgor is maintained through the uptake of water, directly driven by the costly transport and deposition of solutes into the vacuole (Fricke & Chaumont, 2005). In tomato (*Solanum lycopersicum*) leaves, the nitrogen source has a substantial impact on the content of the main cellular soluble compounds (e.g. inorganic ions and organic acids) (Kirkby & Mengel, 1967; Poucet et al., 2021), which are assumed to be stored in the vacuole. The fact that the impact of the nitrogen source varied according to leaf developmental stage raised the question of the role played by vacuole expansion in response to ammonium.

Ammonium (NH_4^+) accumulates inside the vacuole owing to its acidic nature. Indeed, direct microelectrode measurements in NH_4^+-supplied *Chara corallina* cells estimated concentrations in the vacuole to be fourfold that found in the cytosol (Wells & Miller, 2000). NH_4^+ storage in the vacuole has thus been proposed as a strategy used by plants to maintain cytosolic NH_4^+ concentrations. The discovery of the function of the Arabidopsis tonoplast-localized receptor-like kinase CAP1 ([Ca2+]cyt-associated protein kinase 1) in the regulation of vacuolar NH_4^+ compartmentation showed the importance of this process. The cap1-1 mutant presented lower net NH_4^+ flux across the tonoplast and enhanced sensitivity to ammonium stress (Bai et al., 2014). Moreover, it was reported that expressing two Arabidopsis tonoplast aquaporins – TONOPLAST INTRINSIC PROTEIN 2;1 (TIP2;1) and TIP2;3 – in *Saccharomyces cerevisiae* facilitated the transport of NH_3 into the vacuole and conferred yeast tolerance to the presence of methylammonium (Loqué et al., 2005). More recently, ammonium stress has been associated with increased tonoplast degradation and lower tonoplast content in Arabidopsis roots (Robert, Yagyu, Koizumi, et al., 2021). Although the vacuole plays a major role in response to ammonium nutrition, the study of metabolism at the subcellular level remains challenging.

In this work, we addressed this question by developing a mathematical model describing the exchange of solutes between the vacuole and the cytoplasm during leaf development in nitrate- or ammonium-grown tomato plants. We measured the expansion of the vacuole, the cytosolic and vacuolar pH, and major metabolites and inorganic ions at the tissue and subcellular levels using non-aqueous fractionation (NAF). Altogether, our results show that pH homeostasis, primary metabolism and inorganic ions interact to restrain vacuole expansion under ammonium nutrition.

RESULTS

Reduced vacuole expansion under ammonium nutrition is associated with higher tonoplastic ΔpH and profound changes in solute composition

To assess vacuole expansion during leaf cell growth according to the nitrogen source supplied, we monitored the growth of the first tomato leaf able to achieve maximal growth, i.e. the fourth leaf to appear. Ammonium nutrition is known to reduce biomass accumulation (Britto & Kronzucker, 2002). This fourth leaf presented a slower growth rate, leading to poorer biomass, under ammonium nutrition compared with nitrate nutrition (Figure 1a,b). However, leaf growth dynamics did not change with the nitrogen source, and growth reached the maximal rate after 21 days, regardless of the nutrition type. Logically, whole-plant biomass was also reduced under ammonium nutrition, an effect that was enhanced with the age of the plant (Figure S1). Chlorophyll content varied similarly under both nutrition regimes (Figure S2), with a slightly higher chlorophyll content under ammonium nutrition, which is generally associated with mild ammonium stress (Sanchez-Zabala et al., 2015).

Fine monitoring of the volume of parenchymal cells and their main subcellular compartments showed that, similarly to leaf growth, cell and vacuole volume followed a sigmoidal curve pattern during leaf development (Figure 1c). Ammonium nutrition significantly affected cell and vacuole volumes, which were decreased by 38% and 32%, respectively, at day 41. In contrast, the volumes of the cytosol and chloroplast were not significantly affected (Figure S3). Accordingly, the reduced size of the vacuole under ammonium nutrition leads to a decreased ratio of vacuole/cytoplasm during the expansion of ammonium-fed cells when compared with nitrate nutrition (Figure S3). Interestingly, vacuole and cell volumes were strongly correlated, regardless of the N source (Figure 1d). Although it is not fully clear whether vacuolar size changes precede or follow cellular size changes (Kaiser et al., 2021; Kaiser & Scheuring, 2020), this result suggests that ammonium nutrition might impact cell growth by affecting vacuole expansion.

To characterize the metabolic status of tomato leaf during its development, we investigated the tissue concentration of the main soluble species likely accumulating in the vacuole (amino acids, main organic acids, free sugars
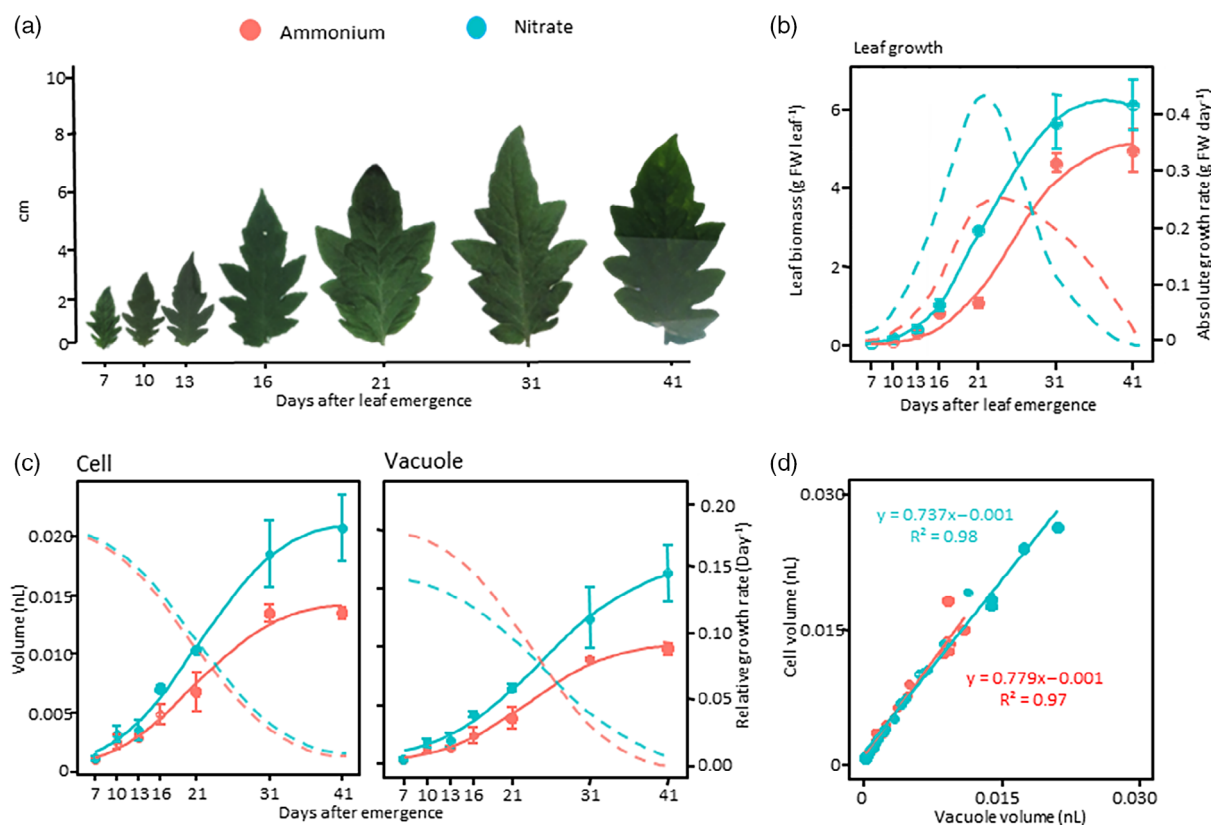
Figure 1. Time-course of leaf fresh weight, and cellular and vacuolar volume throughout leaf development in tomato (*Solanum lycopersicum*) plants grown with ammonium (red) or nitrate (blue) as the nitrogen source. (a) Representative images of the terminal leaflet of the fourth leaf during its development. (b) Leaf growth curve. Continuous lines represent regression analysis using a three-parameter logistic function. Dashed lines represent the absolute growth rate (AGR). (c) Time course of leaf parenchyma cell and vacuole volume. Continuous lines represent regression analysis using a three-parameter logistic function. Dashed lines represent relative growth rate (RGR). (d) Correlations between cell and vacuole volume for plants fed with ammonium (red) and for plants fed with nitrate (blue).

and inorganic ions) (Figures S4 and S5), protein, starch, total C and N contents (Figure S2) and the activity of enzymes involved in central metabolism (Figure S6). Unidimensional clustering analysis highlighted patterns in the investigated compounds that were linked to nitrogen source and leaf development (Figure 2a). Briefly, organic acids (malate and citrate), Mg^{2+}, SO_4^{2-}, NO_3^- and Ca^{2+} predominantly and gradually accumulated under nitrate nutrition. Conversely, the contents of NH_4^+, starch and free hexoses and protein were higher under ammonium nutrition, when the growth rate increased exponentially (13–21 days). Total amino acids, Cl^- and HPO_4^{2-} contents were also higher under ammonium nutrition. Amino acids and Cl^- were accumulated primarily in young expanding leaves, whereas HPO_4^{2-} accumulated in older leaves. Finally, Na^+, K^+, protein, sucrose and chlorophyll contents formed a cluster with few nitrogen-source differences during leaf growth.

Plant cells expand through the continuous deposition of solutes in the vacuole to maintain osmotic pressure, resulting in the inward flow of water (Fricke & Chaumont, 2005). The energization of vacuolar transport partly relies on the ΔpH established across the tonoplast (Rea & Sanders, 1987). We measured cytosolic and vacuolar pH using 2′, 7′-bis-(2-carboxyethyl)-5-(and-6)-carboxyfluorescein (BCECF), a pH-sensitive fluorescent dye (Martinière et al., 2013; Swanson & Jones, 1996). Ammonium nutrition led to significant acidification of the vacuole, with a pH of 5.5 ± 0.1 compared with 6.4 ± 0.1 for nitrate nutrition (Figure 2b). However, the cytosolic pH was maintained at around 6.8 under both conditions, resulting in a ΔpH between the vacuole and the cytosol of 1.2 for cells of ammonium-fed plants and 0.4 for cells of nitrate-fed plants. As NH_4^+ supply is known to acidify the external medium of the cell (Hill et al., 2002), we also extracted apoplastic fluids by infiltration–centrifugation and measured their pH (Figure 2c). As expected, the apoplastic pH was more acidic (pH 5.8 ± 0.1) under ammonium nutrition than under nitrate nutrition (pH 6.4 ± 0.03).

A two-compartment model of solute distribution at thermodynamic equilibrium

Summing the soluble compounds (Figure 3) revealed that the total content of organic and inorganic compounds was
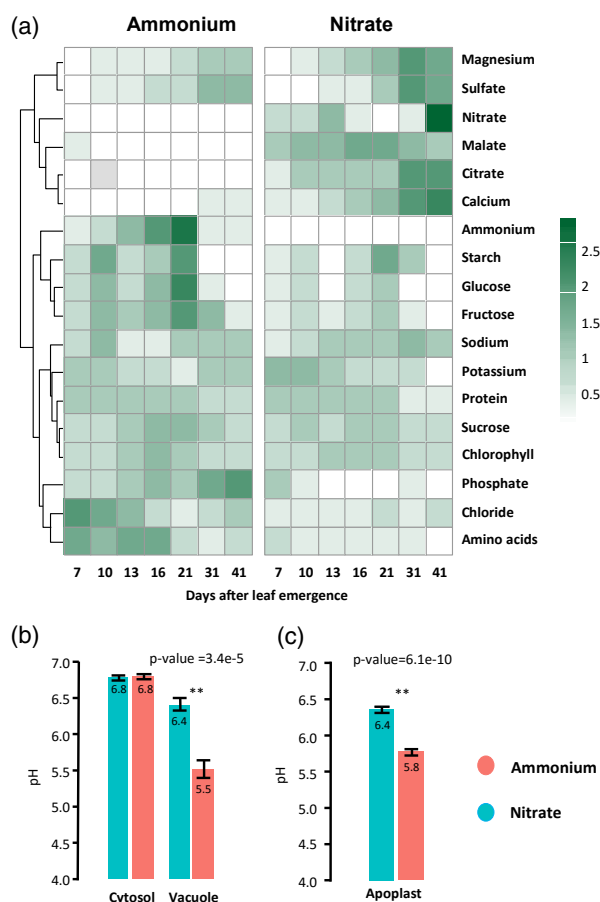
Figure 2. Hierarchical clustering of metabolites and inorganic ion accumulation throughout leaf development in *Solanum lycopersicum* (tomato) plants grown with ammonium or nitrate as the nitrogen source and *in vivo* intracellular pH measurement. (a) Heat map representation of metabolites and inorganic ions obtained after unidimensional hierarchical clustering using the PHEATMAP package in R 1.0.12. Columns correspond to the seven developmental stages and show the mean-centered values ($n = 3$) of the different compounds determined in the study. (b) Vacuolar and cytosolic pH measurement based on BCECF signal. Values represent means ± SEs ($n = 12$ leaves, each replicate corresponding to average of 10 measurements per leaf section). (c) Apoplast pH in tomato leaves fed with ammonium or nitrate as the unique source of nitrogen (values represent means ± SEs, $n = 20$). Significant differences between ammonium and nitrate treatments in panels (b) and (c) are highlighted with asterisks (**$P < 0.01$).

Figure 3. Comparison between experimentally measured and calculated osmolality of tomato leaves grown with ammonium or nitrate as the nitrogen source. The continuous green line represents the osmolality measured with an osmometer. The purple line represents the osmolality predicted by summing the solute contents measured in bulk tissue, expressed in mmol g^{-1} FW, and considering the tissue density (*d*) equal to 1 g FW mL^{-1}. Values represent means ± SDs ($n = 3$).

higher when plants were cultivated in the presence of nitrate as the nitrogen source, suggesting an increase in cell osmolarity. Osmolarities were also deduced from osmolality values measured with an osmometer. The values thus estimated were in the same order and increased similarly in both conditions, from 246 ± 3 to 364 ± 19 mOsmol L^{-1} with ammonium, and from 262 ± 11 to 328 ± 10 mOsmol L^{-1} with nitrate. This result suggests that growth impairment under ammonium conditions was not a consequence of a change in total osmolarity. It raises the question of the subcellular distribution of organic and inorganic compounds and the impact on their cytosolic
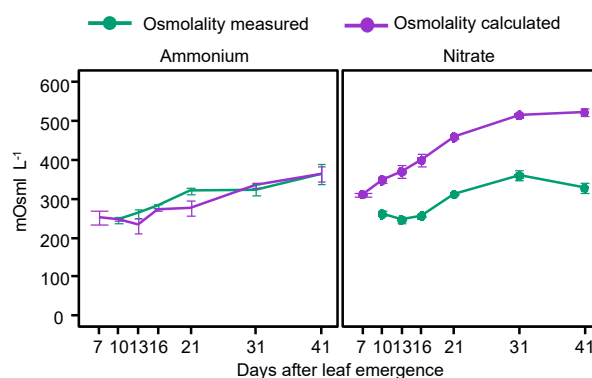
and vacuolar concentrations that could influence the osmolarity of these two compartments, and thus molecule and water fluxes.

Non-aqueous fractionation has been developed to estimate the subcellular distribution of metabolites, classically among the cytosol, the plastids and the vacuole (Destailleur et al., 2021; Krueger et al., 2011). When applied to tomato leaf, it was possible to resolve the vacuole and the cytosol in 21-, 31- and 41-day-old leaves (Table S1), but not in the younger leaves, probably because their cells were too small.

To circumvent the lack of experimental data for young leaves, we created a mathematical model by integrating biochemical and morphometrical data. This model depicted tomato leaf parenchyma as a unique cell with a vacuole and a homogeneous cytoplasm, in which the cytosol, mitochondria and chloroplasts were not distinguished, thus ignoring potential exchanges between these organelles and the cytoplasm.

The model consists of a set of equations describing the concentrations of the 14 major molecules studied within the vacuole and the cytoplasm, taking into account the volume of the respective compartments, the molecule content in the tissue and their transport mechanisms. Amino acids, accounting for less than 7% of total osmolarity with ammonium and 2% with nitrate (see experimental data available online), were neglected in this model. For each compound, the equations were parameterized based on the literature regarding: (i) the driving forces involved in vacuolar transport, i.e. ΔpH (pH$_{vacuole}$ – pH$_{cytoplasm}$) and the electric potential difference ($\Delta\Psi$, V$_{vacuole}$ – V$_{cytoplasm}$) across the tonoplast; and (ii) the stoichiometry of the transport (Table S2). The core skeleton of each equation is

based on the diffusion (for channels) or co-transport (for carriers) at thermodynamic equilibrium, i.e. assuming the transport fluxes are infinitesimally small compared with the transport capacity of carriers (for details, see Appendix S1). As a result of this near-equilibrium assumption (see Appendix S2), the model did not allow the involvement of two different transporters for the same molecule, thus preventing the occurrence of ion cycling across the tonoplast. The model was constructed considering channels for malate, citrate, NH_4^+, SO_4^{2-}, Cl^- and PO_4^{2-}, and H^+ antiporter for hexoses, sucrose, K^+, Na^+, Ca^{2+}, Mg^{2+} and NO_3^- (Table S2). Transport mechanisms were selected based on our current knowledge of vacuolar transport mechanisms in leaves, and taking into consideration the need for a positive net flux of osmolytes into the vacuole to enable water uptake and promote its elongation during leaf expansion (Fricke & Chaumont, 2005; Kaiser & Scheuring, 2020). Equations and parameter settings are listed in Tables S3–S5.

Moreover, some ions such as malate, Ca^{2+} and different forms of phosphate are known to form osmotically inactive complexes when their concentration is above maximum solubility. Solute complexation can affect osmolality and the distribution of solutes across the tonoplast. For this reason, we extensively reviewed the constant of solubility product (K_{sp}) of various ion associations that are most likely to occur in cells. We considered the formation of seven different complexes, the K_{sp} values of which are listed in Table S6. All this information was considered to define three models, the first model with no complex formation (model 1) and two others in which we assumed that some of these compounds would be forming complexes, either in both compartments (model 2) or solely in the vacuole (model 3).

Constraint-based optimization and experimental validation of the model

The cytoplasmic and vacuolar concentrations of major soluble compounds (ions, organic acids and soluble sugars) were simulated with the three models from the measured tissue contents using subcellular volumes and the ΔpH across the tonoplast. The system of equations was first solved for the three late developmental stages (in 21-, 31- and 41-day-old leaves) for which we had subcellular data, assuming a succession of states close to thermodynamic equilibrium. The initial parameterization of the models (model 1) left one parameter free in the equations, i.e. the transmembrane electrical potential across the tonoplast ($\Delta\Psi$). It was optimized to satisfy the electroneutrality of both vacuole and cytoplasm (see Experimental procedures). In the case of models 2 and 3, $\Delta\Psi$ and ionic complex abundances were optimized by least-squares minimization of both the charge imbalance within each compartment and the solubility product of the free ionic

concentrations (see equation in Table S4 and Experimental procedures). The formation of ionic complexes significantly improved the goodness of fit compared with the parameterization without complexes, even though it was almost the same regardless of the localization of complexes (Figure 4a). Indeed, the addition of complex formation in our model led to a reduction in the subcellular concentrations of (Figures S7, S8 and 5c, referring to models 1 to 3, respectively). Therefore, the estimated leaf osmolality (equations in Table S4) was closer to the osmolality measured experimentally with an osmometer (Figure 4b). This was particularly evident when NO_3^- was the nitrogen source. In these plants, the soluble concentration of Ca^{2+}, and to a lesser extent that of HPO_4^{2-}, decreased strongly in both compartments because of complex formation (Figures 5c, S7 and S8).

To validate our model, the predicted subcellular concentrations were compared with the values obtained with NAF at 21, 31 and 41 days (Table S1). Considering plants grown with ammonium, the three models simulated cytoplasmic and vacuolar concentrations in the range of experimentally determined concentrations, with the exception of Cl^- and sucrose, the cytoplasmic concentrations of which were underestimated (Figures S9, S10 and S11). In contrast, in plants grown under nitrate nutrition, the cytoplasmic concentrations of Mg^{2+}, Ca^{2+}, SO_4^{2-} and malate were all overestimated in model 1 (Figure S9), but also in model 2 (Figure S10), despite that it improved the goodness of fit through a better estimation of cell osmolarity (Figure 4a). In general, simulations were greatly improved with model 3 for both types of nitrogen nutrition, with better linear correlation between predicted and experimentally determined results (Figure 4c), in terms of R^2 (0.87), slope (0.90) and intercept (3.24). With model 3, total vacuolar and cytosolic concentrations were remarkably close to those determined experimentally (Figure S11), except for magnesium. This was further illustrated by the χ^2 score, the discrepancy between the NAF-derived and modeled concentrations being lower when complex formation occurred only in the vacuole (χ^2 score of 772 with model 3 vs 7373 with model 2). Interestingly, the modification of model 3 by replacing the transport mechanism for several ions (Cl^-, NO_3^-, organic acids or K^+) did not improve the model (Table S7). Therefore, the initially defined model 3 (Figure 5a), which best fits the experimental data, was retained to predict subcellular metabolite concentrations during leaf development as a function of the nitrogen source supplied.

Lower vacuolar flux of solutes under ammonium nutrition but with higher energy cost

Given the great predictability of model 3 (Figure 5a), involving complex formation in the vacuole only, we analyzed the model output for subcellular concentrations of
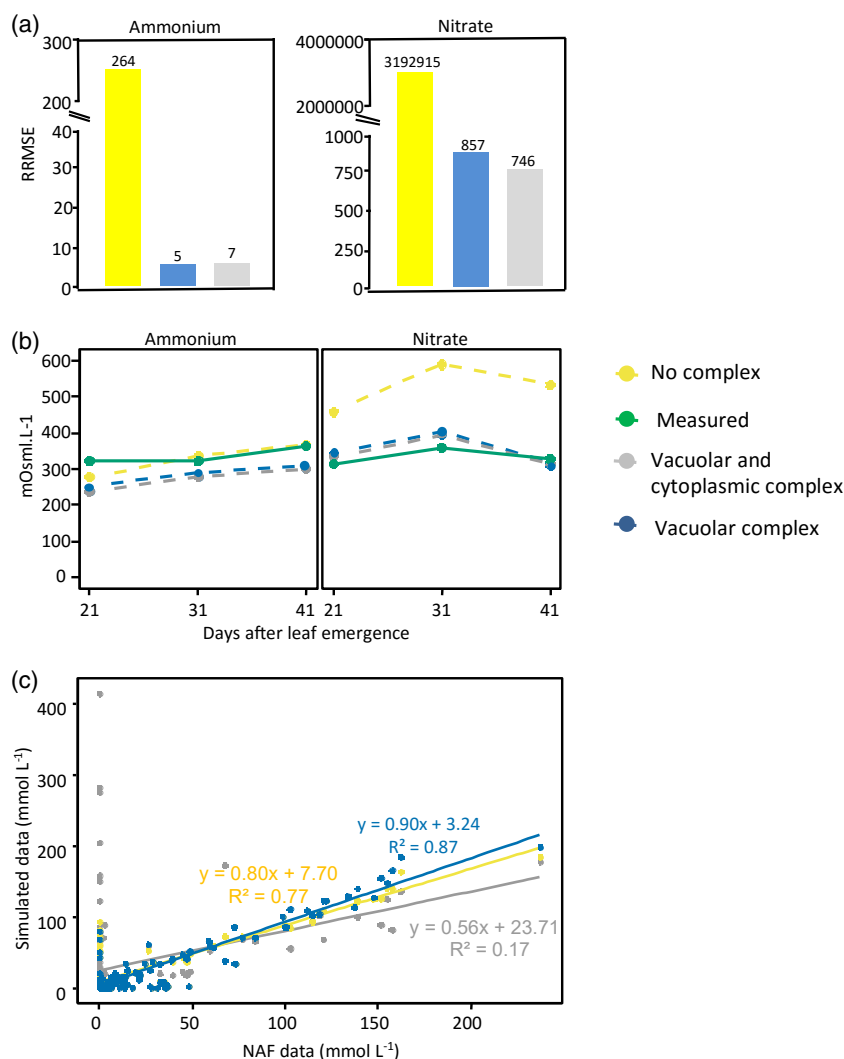
Figure 4. Comparison of the fits and validation, over the three stages (21J, 31J and 41J), of the vacuolar ion complex parameterization (model 3) as the best fit. Three models were used to fit our data: model 1 (yellow), model 2 (gray) and model 3 (blue). (a) Mean value of goodness of fit, expressed as the relative root mean squared error (RRMSE) of various parameterizations related to electroneutrality, complex formation and osmolality (as described in Experimental procedures). (b) Comparison between simulated and experimentally measured osmolality in leaves of *Solanum lycopersicum* (tomato) plants grown for 21, 31 and 41 days with ammonium or nitrate as the nitrogen source. The continuous green line represents whole-tissue osmolality measured with an osmometer ($n = 3$). The dashed lines represent tissue osmolality predicted as the sum of means ($n = 200$) of inorganic ions and organic metabolites accumulated in the vacuole and cytoplasm under soluble form (c). Comparison between experimentally determined concentrations of compounds measured by non-aqueous fractionation (NAF) and predicted data from the parameterizations of the three models.

each compound at seven developmental stages. Accordingly, the coefficient of variation over the 200 best-scoring optimizations showed that subcellular concentrations of most compounds were statistically reliable, especially for vacuolar concentrations, where the coefficient of variation was always lower than 23% (Figure S12). The results (Figure 5c) showed that inorganic ions and organic species were mostly located within the vacuole, with concentrations always higher than in the cytosol. As expected, inorganic N was mostly accumulated in the vacuole. The maximal concentrations for NH_4^+ were estimated to be 3.3 ± 0.2 mM in the cytoplasm and 58 ± 3 mM in the

vacuole at day 21 under ammonium nutrition. These results are consistent with the direct measurement of NH_4^+ with a microelectrode in *C. corallina*, which reached 30.8 mM in the vacuole and 7.3 mM in the cytosol after 2 days of incubation with 1 mM NH_4^+ (Wells & Miller, 2000).

Interestingly, in the early stages of leaf development, the model showed that malate was present mainly in soluble form and that it contributed significantly to osmolality. In contrast, in older leaves, it was complexed with Ca^{2+}, up to 73%. Consequently, in 31- and 41-day-old leaves, the contribution of malate to osmolality was lower than 12% (Figure 5b) under nitrate-based nutrition. Access
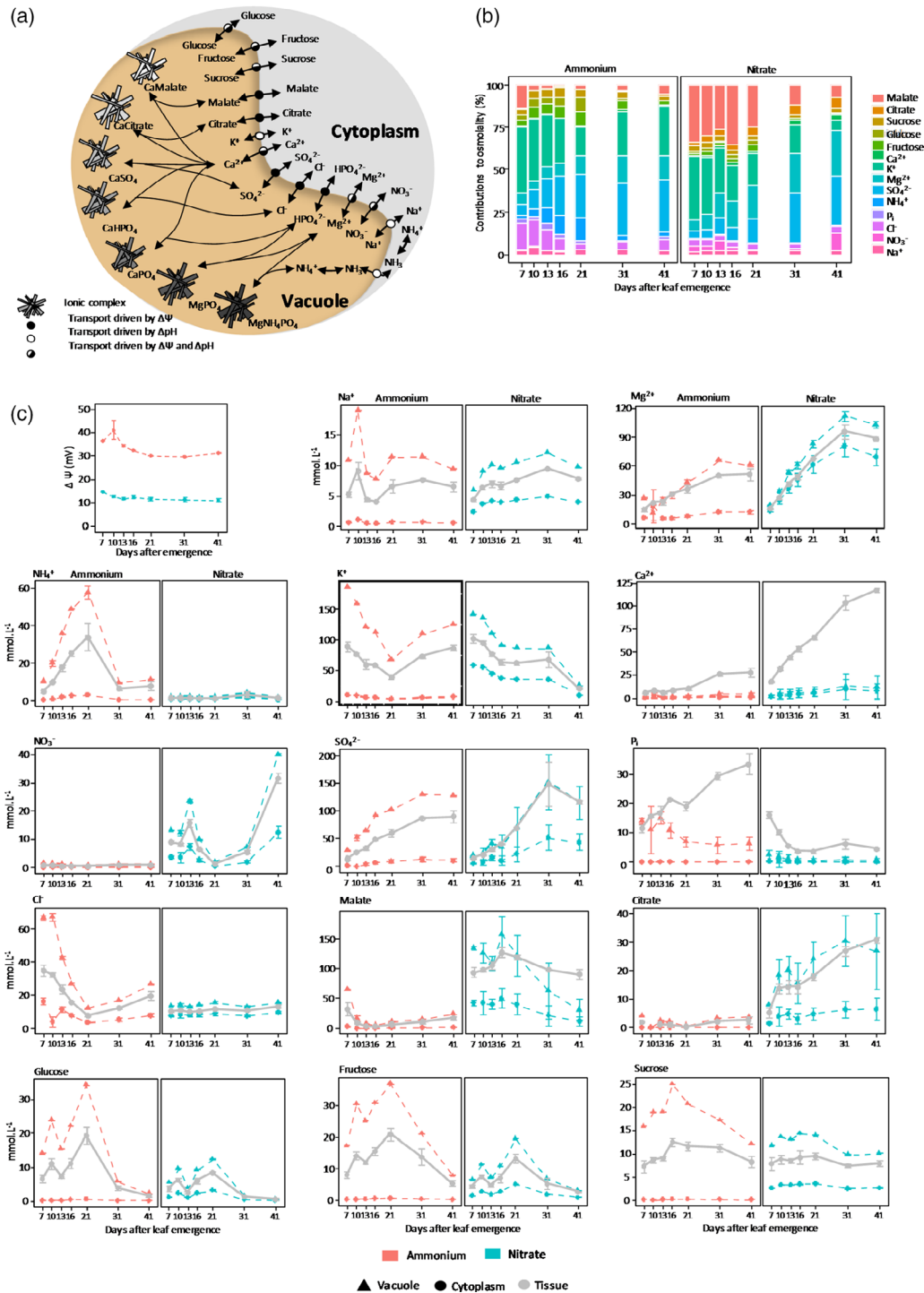
1020   *Théo Poucet* et al.

Figure 5. Predicted ΔΨ and subcellular concentration of organic and inorganic compounds throughout leaf development in *Solanum lycopersicum* (tomato) plants grown with nitrate or ammonium as the nitrogen source. (a) Schematic network of subcellular compartmentation and ionic complexation of solutes in a tomato leaf cell (model 3). The subcellular distribution of 14 inorganic and organic soluble compounds is dependent on their respective transporters. Channel transporters (black circles) are energized by ΔΨ whereas H⁺-antiport transporters are energized by ΔpH (white circles) or ΔΨ and ΔpH (black-and-white circle). The ↔ arrows indicate the thermodynamic equilibrium for each chemical species across the tonoplast and under complex form (symbolized by crystal structures) into the vacuole. (b) Predicted relative contribution of individual solutes to total osmolality, considering tissue density as 1 g FW mL⁻¹. (c) Predicted ΔΨ across tonoplast and vacuolar (triangle) and cytoplasmic (circle) concentration of soluble organic and inorganic compounds in leaf development in plants grown with ammonium (red) or nitrate (blue) as the nitrogen source. Gray line represents experimentally determined content in bulk tissue multiplied by the tissue density ($n = 3$). In panels (b) and (c), values represent means ± SDs of the 200 best-scoring combinations of parameters obtained by least-square minimization using a genetic algorithm with randomized initial conditions, as described in the Experimental procedures.
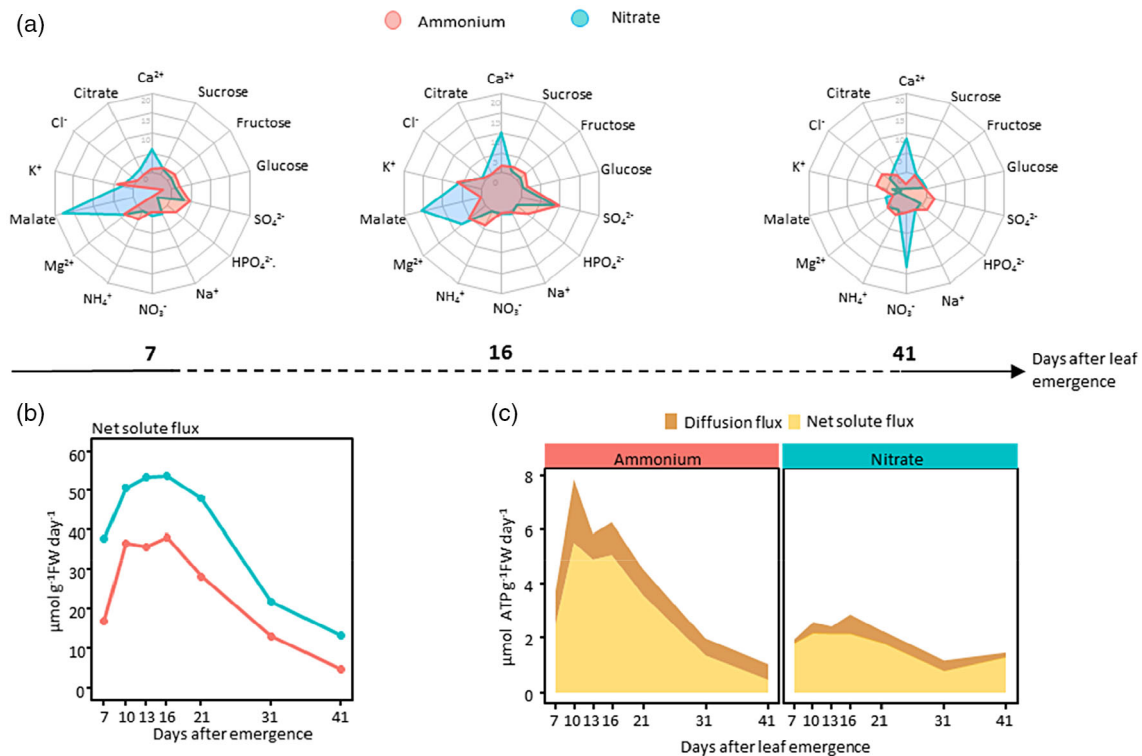
Figure 6. Reduced vacuolar expansion under ammonium nutrition associated with lower solute vacuolar flux at higher energy cost. (a) Radar representation of simulated individual solute vacuolar net fluxes (expressed as $\mu mol\ g^{-1}$ FW day^{-1}) at three representative leaf developmental stages in plants grown with ammonium (red) or nitrate (blue) as the nitrogen source. (b) Modeled evolution of the net flux of vacuolar solutes. (c) Modeled energy cost of solute net transport and leakage when plants are grown with ammonium or nitrate as the unique nitrogen source (expressed in μmol ATP equivalent to g $FW^{-1}\ day^{-1}$). Vacuolar solute flux and associated energy cost were calculated as detailed in Appendix S1, with the model allowing ion complexation exclusively in vacuole.

to the subcellular concentrations at every developmental stage allowed us to calculate the net uptake of solutes into the vacuole, considering: (i) the evolution of vacuolar volume, i.e. the expansion rate (Figure S13); (ii) the variation in concentration in the vacuole, i.e. the accumulation rate (Figure S13), calculating the derivative of the curve fit of total concentrations (Figure S14); and (iii) the diffusion flux across the tonoplast (Figure S13) (for details, see Appendix S1). Under both nutrition types, the individual net solute fluxes were higher (Figures 6a and S13) when the vacuolar relative growth rate was maximal (between 7 and 21 days; Figure 1c), and then sharply decreased until the end of leaf development. The most striking difference between treatments was the higher net flux of Ca^{2+} and malate under nitrate nutrition (Figure 6a). Accordingly, in agreement with lower vacuole expansion under ammonium nutrition (Figure 1c), the cumulated net flux of solutes into the vacuole was always lower (27%–62%) under ammonium nutrition than under nitrate nutrition (Figure 6b).

Finally, we estimated the energy cost of vacuole expansion under both nutrition regimes by calculating the cost of solute fluxes in terms of ATP (Figure 6c) (for

details, see Appendix S1 and Figure S15). Despite the lower net solute flux (Figure 6b), the higher tonoplast ΔpH and $\Delta\Psi$ of NH_4^+-fed plants implied that solute transport was energetically more expensive than in NO_3^--fed plant cells (Figure 6c). Indeed, the ATP needed to sustain the vacuolar fluxes under ammonium treatment was approximately twice as high between days 7 and 21 compared with nitrate treatment. Finally, upon leaf growth arrest, the energy cost of vacuolar fluxes was low and similar for both nutrition regimes. It is worth noting that changing the parameterization of individual transport mechanisms (as mentioned in Table S7) did not have a significant impact on the energy cost of vacuolar fluxes. Accordingly, the ATP cost always remained higher under ammonium nutrition when compared with nitrate nutrition (Figure S16).

DISCUSSION

Providing NO_3^- or NH_4^+ to a plant induces drastic changes in solute accumulation as a result of profound metabolic adaptation and altered ionic balances (Britto & Kronzucker, 2002). In addition, there is a growing body of evidence linking the nitrogen source to differential cell

growth (Liu et al., 2013; Ötvös et al., 2021; Podgórska et al., 2017; Robert, Yagyu, Lascano, et al., 2021; Walch-Liu et al., 2000). However, the reasons behind this phenomenon remain unclear. Vacuole expansion is essential to cell growth and is critical for NH_4^+ sequestration inside the vacuole to promote ammonium tolerance in plant (Bai et al., 2014; Loqué et al., 2005). In this context, cytological monitoring of tomato leaf development suggests that the perturbation of vacuole expansion might play a major role in the reduction of cell growth (Figure 1).

Mathematical modeling to predict solute distribution across the tonoplast

The transport of solutes across the tonoplast and their vacuolar concentration depends on the type of vacuolar transport, the total solute tissue content, the ΔpH across the tonoplast, the membrane potential ($\Delta\Psi$) and the abundance of ionic complexes. Optimization of the latter two parameters helped match the predicted subcellular concentrations with the data obtained experimentally, i.e. tissue osmolality and subcellular concentrations obtained via NAF for leaves on days 21, 31 and 41 after appearance. The formation of ionic complexes, which is commonly associated with the maintenance of ion homeostasis in plants (Volk et al., 2002), significantly improved the quality of model predictions, especially when constraining it to the vacuole. In agreement with this model, it has been shown that calcium oxalate crystals accumulate specifically in the vacuole (Nakata, 2012). The most significant discrepancies found between predicted and experimental data concerned Cl^- and sucrose (Figure S11). Regarding sucrose, the model overestimated its concentration in the vacuole independently of the nitrogen source (Figure S11). An essential metabolic activity inside the vacuole is sucrose hydrolysis by acid invertase, which was higher under ammonium nutrition (Figure S6), as also reported in *Beta vulgaris* (Raab & Terry, 1995). This activity may affect the sucrose gradient and its transport across the tonoplast (Beauvoit et al., 2014). Importantly, such activity conflicted with the present model parameterized at equilibrium, resulting in the inaccurate prediction for sucrose location but not for the other sugars tested.

Overall, our model fitted the experimental data very well at three developmental stages of the leaf, from 21 to 41 days ($R^2 = 0.87$, slope = 0.90; Figure 4) and proved to be an outstanding tool to predict the subcellular distribution of solutes. Providing estimates for 14 major solutes in the early stages was particularly interesting, as experimental data could not be obtained for these stages. Importantly, this made it possible to calculate the total net flux of vacuolar solutes required for cell expansion as well as the associated energy cost (Figure 6).

Vacuole acidification: an essential but costly strategy for maintaining cytosolic pH homeostasis under ammonium nutrition

One of the well-known effects of ammonium nutrition is the acidification of the external cell medium to ensure cytosolic pH homeostasis (Hachiya et al., 2012; Meier et al., 2020). Together with a more acidic apoplast, we found significant acidification of the vacuole under long-term ammonium nutrition. This result is not in agreement with the increase in vacuolar pH reported for cells transiently exposed to high external NH_4^+ concentrations (Gerendás & Ratcliffe, 2000; Roberts et al., 1982; Roberts & Pang, 1992). In short transient experiments, rapid alkalinization corroborates the mechanism of NH_4^+ vacuolar transport, which is based on 'ion trapping' (Britto et al., 2001). Here, during prolonged exposure to high levels of NH_4^+, the pH variations observed within leaves reflect the integrative cell metabolic response to cope with acidity over long periods. It is generally assumed that NH_4^+ assimilation produces protons within the cytosol, whereas NO_3^- assimilation consumes protons (Britto & Kronzucker, 2005; Hachiya et al., 2021).

The maintenance of cytosolic pH under ammonium nutrition is possible thanks to the joint functioning of the biochemical and biophysical pH-stat mechanisms. In line with the hypothesis of a biochemical mechanism to scavenge H^+ in the cytosol, and as previously reported (Poucet et al., 2021), we also observed lower phosphoenolpyruvate carboxylase (PEPC) enzyme activity together with higher malic enzyme (ME) activity under ammonium nutrition (Figure S6). The co-regulated activity of both enzymes is consistent with the low levels of malate commonly observed in leaves under ammonium nutrition (Hachiya et al., 2012; Kirkby & Mengel, 1967; Poucet et al., 2021; Vega-Mas et al., 2019), including in the present work. Vacuolar and apoplastic acidification may participate in the biophysical pH-stat mechanism via the regulation of the net translocation of H^+ out of the cytosol, suggesting the activation of proton pumps to ensure vacuolar H^+ uptake. The long-term ammonium nutrition effect on vacuolar pH was previously investigated by ^{14}N nuclear magnetic resonance (NMR) spectroscopy in the Norway spruce (*Picea abies*; Aarnes et al., 2007), a conifer well adapted to high NH_4^+ content in the soil (Aarnes et al., 2007; Kronzucker et al., 1997). However, no significant difference was found between seedlings growing on NH_4^+ and NO_3^- as the nitrogen source (Aarnes et al., 2007). The vacuole acidification observed in our work is probably helping to preserve cytosol integrity in tomato, which, unlike Norway spruce, is an ammonium-sensitive plant (Kirkby & Mengel, 1967; Poucet et al., 2021; Vega-Mas et al., 2017).

In our model, after constraint-based optimization, the higher ΔpH in NH_4^+-fed plants ended up in a higher

transmembrane potential ($\Delta \Psi$v-c) across the tonoplast compared with NO_3^--fed plants. ΔpH energizes H^+-antiport transporters, which mainly translocate positively charged compounds such as K^+ or Ca^{2+}. A higher $\Delta \Psi$ is thus necessary to improve the transport of counter ions in order to preserve electroneutrality. The model proposed by Lobit et al. (2006), to explain malate accumulation in fruit, indicates that the electromotive force would decrease as the vacuolar pH decreases. This discrepancy with our results comes from the constraints that they imposed, i.e. the pumps as well as the transporters operate at equilibrium, whereas only the transporters are constrained to equilibrium in our model. The higher ΔpH and $\Delta \Psi$ in NH_4^+-fed plants elicit important consequences for vacuolar performance. First, it increases the sequestration capacity of the vacuole for different solutes, thereby augmenting the intensity of leaks through the tonoplast. Second, it increases the energy cost of solute transport into the vacuole. A study in protoplasts of bean (*Vicia faba*) leaf mesophyll based on similar calculations also evidenced that the energy cost of H^+ influx increased when ΔpH across the plasma membrane was higher (Wegner & Shabala, 2019). Therefore, decreasing the vacuolar pH appears to be an efficient strategy to preserve cytoplasm homeostasis under ammonium nutrition. However, it involves an energy trade-off as it dramatically increases the energy cost of

solute fluxes during vacuole expansion (Figure 6c), potentially impacting leaf growth and biomass accumulation.

Depletion of organic acids under ammonium nutrition, as a consequence of the decreased use of sugars, impacts vacuole growth

The dramatic depletion of leaf organic acid (malate and citrate) content under ammonium nutrition is well known. This decrease has been associated with the requirement of carbon skeletons to sustain high NH_4^+ assimilation rates and with the regulation of cytosolic pH through the biochemical pH-stat mechanism (de la Peña et al., 2019; Hachiya et al., 2012; Kirkby & Mengel, 1967; Pasqualini et al., 2001; Poucet et al., 2021; Van Beusichem et al., 1988). Our model revealed a critical aspect of organic acid depletion: its contribution to vacuole expansion. Indeed, although cell osmolality did not differ between NO_3^-- and NH_4^+-fed plants (Figure 4b), the model showed much higher net fluxes of solutes across the tonoplast under nitrate nutrition, in particular for malate and citrate (Figure 6a), major vacuolar osmolytes that promoted vacuole expansion under nitrate nutrition.

Interestingly, the K^+ concentration was very low in the cytosol of plants grown under ammonium nutrition (Figure 5), suggesting an early limitation in the activity of pyruvate kinase (PK). In fact, the measured and estimated
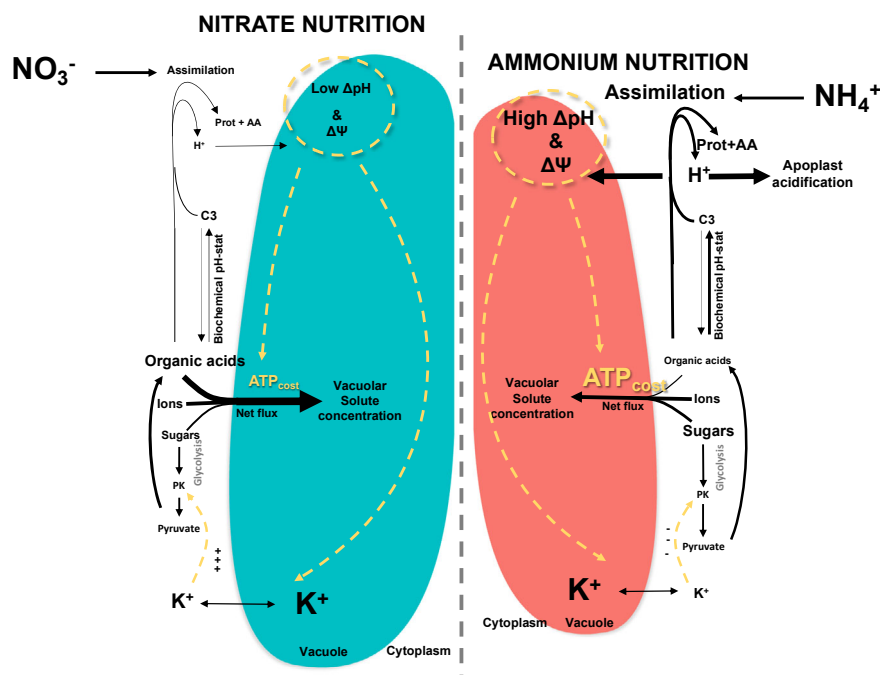

Figure 7. Reduction of cell growth in tomato leaf in response to ammonium feeding: a proposed model of the regulation of metabolism. Providing ammonium as the exclusive source of nitrogen provoked the acidification of the vacuole that together with proton extrusion to the apoplast and the biochemical pH-stat mechanism cooperate to maintain cytosolic pH. Vacuole acidification entailed a higher $\Delta \Psi$ that, coupled with the depletion of organic acids, provoked a reduction in import fluxes into the vacuole and an increase in the energy cost of solute transport across the tonoplast under ammonium nutrition. Moreover, we also propose a mechanism for the observed accumulation of sugars under ammonium nutrition associated with the decrease in pyruvate kinase activity, owing to the decrease in cytosolic potassium concentration.

K$^+$ concentrations (from 3.9 to 10.8 m$_M$) were in the Michaelis constant (K_M) range of this enzyme (Baysdorfer & Bassham, 1984). On the contrary, under nitrate nutrition, K$^+$ concentrations, although decreasing from 58 m$_M$ in the very young leaf to 35 m$_M$ in the mature leaf, were still saturating, thus promoting glycolytic flux. Consistently, we also found a significant although limited decrease in PK activity under ammonium nutrition (Figure S6). Both the PK inhibition and down-modulation might limit the glycolysis and downstream pathways, and therefore reduce energy production. This hypothesis of a bottleneck induced by ammonium in organic acid metabolism is reinforced by the fact that PEPC activity was reduced and ME increased. Moreover, partial PK inhibition may also explain the accumulation of soluble sugars often observed in leaves under ammonium nutrition (Poucet et al., 2021; Setién et al., 2013; Vega-Mas et al., 2017; Walch-Liu et al., 2000) (Figure S6). Altogether, ammonium nutrition leads to a paradox, in which the use of photosynthesis products for leaf growth is limited whereas the energy costs of growth increase, especially those associated with vacuole expansion (Figure 6c).

CONCLUSION

The understanding of the role of the vacuole in response to ammonium nutrition is generally limited because of a lack of knowledge about subcellular concentrations of metabolites. In this work, we combined *in vivo* pH measurement, NAF and mathematical modeling to estimate the subcellular concentrations of ions and organic acids during the development of the tomato leaf according to the nitrogen source provided: nitrate or ammonium. As summarized in Figure 7, vacuole acidification is an essential mechanism that cooperates with proton extrusion and biochemical pH-stat to maintain cytosolic pH under ammonium nutrition. Together with the depletion of organic acids, vacuole acidification entailed a reduction of import fluxes into the vacuole and an increase in the energy cost of solute transport across the tonoplast under ammonium nutrition. Additionally, estimates for cytoplasmic K$^+$ concentration pointed to a possible, although partial, decrease in the activity of pyruvate kinase that could contribute to limit the use of sugars via glycolysis. Altogether, our work provides an explanation for cell growth reduction in tomato leaf under ammonium nutrition. It paves the way to further investigate the molecular actors involved in this mechanism that may be useful to improve plant ammonium tolerance, which in turn is pivotal to reduce the impact of nitrogen fertilization on the environment.

EXPERIMENTAL PROCEDURES

Growth conditions and experimental design

The germination of tomato (*S. lycopersicum*, cv. M82) seeds was conducted in trays with perlite:vermiculite 1:2 (v:v) inert substrate mixture and watered with deionized water. The trays spent 14 days in a growth chamber with the following environmental conditions: light intensity of 350 μmol m^{-2} sec^{-1} with a 14-h light/10-h dark photoperiod, 60%/70% relative humidity and 23°C day/18°C night conditions. Six hundred homogeneous seedlings were transferred to 500-ml pots (with one seedling per pot) with perlite:vermiculite 1:2 (v:v) and set up in a glasshouse (Greenhouse Service, SGIker, UPV/EHU). After 35 days, plants were transferred to 2.8-L pots. The glasshouse conditions had a 14-h day/12-h night photoperiod, with the support of additional light sources ensuring a minimum light intensity of 200 μmol m^{-2} sec^{-1}. Temperature and relative humidity were 25°C/18°C and 50%/60%, respectively, during the day/night. Plants were irrigated three times a week with a nutrient solution adjusted to pH 6 that contained macronutrients (1.15 m$_M$ K$_2$HPO$_4$, 0.85 m$_M$ MgSO$_4$, 0.7 m$_M$ CaSO$_4$, 2.68 m$_M$ KCl, 0.5 m$_M$ CaCO$_3$, 0.07 m$_M$ NaFeEDTA) and micronutrients (16.5 μ$_M$ Na$_2$MoO$_4$, 3.5 μ$_M$ ZnSO$_4$, 3.7 μ$_M$ FeCl$_3$, 0.47 μ$_M$ MnSO$_4$, 0.12 μ$_M$ CuSO$_4$, 16.2 μ$_M$ H$_3$BO$_3$, 0.21 μ$_M$ AlCl$_3$, 0.126 μ$_M$ NiCl$_2$ and 0.06 μ$_M$ KI). Nitrogen was applied at a final concentration of 15 m$_M$ in two different forms that corresponded to 100% ammonium, applied as 7.5 m$_M$ (NH$_4$)$_2$SO$_4$, and 100% nitrate, applied as 7.5 m$_M$ Ca(NO$_3$)$_2$. To compare both nutrient regimes, in the main experiment, nitrate nutrition was supplemented with 7.5 m$_M$ CaSO$_4$ to equilibrate the sulfate supplied in the ammonium treatment. Overall, 300 plants were grown for each treatment.

Plants were monitored daily to register and tag the appearance of the fourth leaf on every plant. Overall, we estimated that when the terminal leaflet of the leaf was 3.5 cm long it corresponded to a 7-day-old leaf, which in turn corresponded to a 30- to 35-day-old plant. With this criterion, and to monitor leaf development according to the nitrogen source provided, we harvested the fourth leaf at seven time points corresponding to 7-, 10-, 13-, 16-, 21-, 31- and 41-day-old leaves. Three or four plants per treatment and time point were harvested to determine biomass parameters (fresh and dry weight) and conduct a cytological analysis. Dry weight was determined after drying the plant material in an oven at 80°C for 72 h.

Sampling and determination of metabolites

For metabolic analyses, three biological replicates were collected per time point, each replicate consisting of a pool of the fourth leaf of 10 plants. To do so, the central vein of the leaves was rapidly removed with a scalpel and the remaining lamina was immediately frozen in liquid nitrogen and stored at −80°C for further analysis. Leaf pools were ground to powder in a tissue lyser (MM 400; Retsch, https://www.retsch.com) at cryogenic temperature. Leaves were harvested between 10 a.m. and 1 p.m.

Metabolites were extracted as described by Luna et al. (2020) from 20-mg aliquots of frozen leaf powder. Total chlorophylls, soluble sugars, malate, citrate, proteins and starch were quantified as described by Poucet et al. (2021). Amino acids were quantified by HPLC fluorometry (Biais et al., 2014).

Extraction, determination and quantification of soluble ions

Aliquots of fresh frozen leaf powder (20 mg) were homogenized with 1 ml of ultrapure water and incubated at 85°C for 10 min. After 10 min of centrifugation at 15 000 **g**, supernatants were removed and filtered through 0.22 μm × 13 mm PVDF filters. Soluble cations and anions were measured by ion chromatography (DIONEX ICS-5000; ThermoFisher Scientific, https://www.thermofisher.com) at the Servicio Fitotrón e Invernadero SGIker, UPV/EHU.

Enzyme activity

Enzymes were extracted as described in Gibon et al. (2004). Activities of malate dehydrogenase (MDH), phosphoenol pyruvate carboxylase (PEPC), pyruvate kinase (PK), acid invertase (AI), fructokinase (FK) and glucokinase (GK) were determined by spectrophotometry using 96-well microplate spectrophotometers, as described by Gibon et al. (2004). Acid invertase was performed after desalting (PD Multitrap G-25; GE Healthcare, http://www.gehealthcare.com). The protocol for measuring NADP-dependent malic enzyme (ME) activity was adapted from Holtum & Winter (1982).

Total carbon and nitrogen

Nitrogen and carbon contents were quantified by the combustion of dry plant material with elemental analyzer Flash EA1112 (ThermoFisher Scientific).

Cytological study

Leaf blade fragments (1–2 mm thick) were placed in 2.5% glutaraldehyde (v/v) in 0.1 M sodium phosphate buffer, pH 7.2, kept at 4°C on ice. During the first hour of fixation, an increasing vacuum (from 800 to 200 mbar) was applied and interrupted every 15 min. Samples were rinsed three times in cold phosphate buffer and treated with 1% tannic acid for 30 min under agitation. After three water rinses, samples were dehydrated by an acetone series. For embedding, samples were placed for 1 h in an acetone:Epon 812 mixture (50:50, v/v; EMBed-812 embedding kit; EMS, https://www.emsdiasum.com) under agitation. After the acetone had evaporated, samples were transferred to 100% Epon 812 mixture and incubated overnight at room temperature. Fixed fragments were placed into silicon molds with fresh Epon solution and polymerization was performed at 70°C for 16 h. Fixed sections were sliced (1 μm) with glass knives and stained with 0.04% (w/v) toluidine blue.

Sections were photographed using a Zeiss Axiophot microscope (https://www.zeiss.com) coupled with a Spot RTKE digital camera. To calculate cell and subcellular volumes, cell, vacuole, cytoplasm, chloroplast and cell wall areas were measured with IMAGEJ (https://imagej.nih.gov/ij/) by manual drawing. The ellipse that corresponded best to the measured areas was computed to provide ellipsis parameters (Figure S3): with a being the semi-major axis and b being the semi-minor axis. Volumes were calculated assuming that the cell and vacuole were prolate spheroids of radius a, b and c (with $a > b = c$) (Beauvoit et al., 2014). We assumed that the cell wall was homogenously distributed around the plasma membrane. For chloroplast volumes, we assumed that they were homogeneously distributed within the cytoplasm. Finally, the cytoplasmic space was determined by calculating the difference between total cell volume and the above calculated volumes for the vacuole, chloroplasts and cell wall. For each biological replicate, subcellular volumes were determined and averaged from six parenchyma cells.

pH measurements

Vacuolar and cytoplasmic pH was determined using the ratiometric fluorescent cell-permeant BCECF-AM dye (CAS117464-70-7; Santa Cruz Biotechnology, https://www.scbt.com) (Martinière et al., 2013). Transversal tomato leaf sections (90 μm thick) were obtained using a vibratome (Microm HM650V, Thermo Scientific). Loading of the dye was performed by incubating the leaf sections for 20 min in dye-loading medium (50 mM 2-(N-morpholine)-ethanesulphonic acid (MES)-TRIS, adjusted to pH 6.5, 135 mM KCl,

100 μM $CaCl_2$, 5 μM BCECF-AM, 0.02% of pluronic acid) at room temperature, in the dark, followed by a 10 min incubation in dye-loading medium without BCECF-AM and pluronic acid. BCECF-AM fluorescence was detected with a ×20 PL-APO objective on a Leica LCS SP2 AOBS confocal microscope (Leica, https://www.leica-microsystems.com) with sequential excitation at 488 nm and 454 nm, and emission was recorded in the 525–550 nm band. Auto-fluorescence of chloroplasts at 600 nm was used to define compartments. As expected, dye was mainly loaded in the vacuole but was also detectable in the cytosol (Giglioli-Guivarc'h et al., 1996). Images were analyzed with FIJI (IMAGEJ). Fluorescence 488/454 ratios were converted into pH values based on the calibration curve made in the occlusive cells of the stomata following the nigericin method (Brauer et al., 1995). To avoid any interference of nutrition type with the dye sensitivity, calibration curves were performed in leaf sections coming from plants grown under ammonium or nitrate conditions, with no difference reported between curves (Figure S17).

Apoplastic fluids were extracted by gentle centrifugation and the apoplast dilution factor was calculated using infiltration with indigo carmine following the method described by O'Leary et al. (2014). Finally, pH was determined with a microelectrode.

Osmolality and osmolarity

Aliquots of 20 mg of frozen leaf powder were homogenized by vigorous shaking with 150 μl of deionized water. Homogenates were centrifuged at 15 000 g for 10 min and osmolality (mOsmol kg^{-1} H_2O) was measured in the supernatants with a Micro-Osmometer Type 13/13DR (Roebling). The osmolarity values were converted to osmolarity (mOsmol L^{-1}) assuming the equivalence between 1 L and 1 kg of water.

Non-aqueous subcellular fractionation (NAF)

The NAF protocol was adapted from Fürtauer et al. (2016), with slight modifications. Frozen leaf powder was freeze-dried for 7 days. A 50-mg portion of powder was suspended in 7 ml of pre-chilled heptane/tetrachloroethylene mixture (ρ = 1.3 g cm^{-3}). After sonication, the suspension was filtered through a nylon mesh (with a pore size of 22–25 μm). The remaining suspension was adjusted to 25 ml with pure heptane and centrifuged at 4800 g for 10 min at 4°C. The pellet was resuspended in 1 ml of pure tetrachloroethylene (ρ = 1.3 g cm^{-3}) and centrifuged at 24 000 g for 10 min at 4°C. The pellet was retained and the supernatant was transferred into a new reaction tube. Densities of the heptane/tetrachloroethylene mixtures for the three following fractions were 1.48, 1.42 and 1.36 g.m^{-3}, respectively. The supernatant of the last fraction was adjusted to 7 ml with pure heptane and centrifuged at 4800 g for 10 min at 4°C. All pellets were resuspended in a heptane/tetra-chloroethylene mixture according to the density of the corresponding fraction, and aliquoted into four subfractions. These subfractions were precipitated by adding pure heptane (ρ = 0.68 g cm^{-3}) followed by centrifugation at 13 100 g for 3 min at 4°C. Samples were dried in a vacuum concentrator (LaboGene, https://www.labogene.com). Aliquots were stored at −20°C to further perform ethanolic extractions for metabolite determination and enzyme extractions (as previously described). Chlorogenic acid, determined by liquid chromatography–mass spectrometry (LC–MS), and mannosidase activity were used as vacuolar markers (Beshir et al., 2019; Sazzad Hossain et al., 2017). Chlorophyll and NADP-glyceraldehyde-3-phosphate dehydrogenase activity were used as chloroplastic markers (Krueger et al., 2011) and phosphoenolpyruvate carboxylase activity was used as a cytosolic marker (Stitt et al., 1989). The cytoplasm concentrations shown in

Table S1 correspond to the merged cytosol and chloroplast concentrations.

Mathematical modeling and model parameter optimization

The summary of transporter characteristics used for model parameterization I presented in Table S2. The set of equations describing the final model are listed in Tables S3 and S4 and was solved by COPASI 4.7 (Hoops et al., 2006) using the constants defined in Table S5. For each optimization set-up, 14 COPASI files corresponding to the seven developmental stages of NH_4^+- and NO_3^--fed plants were generated. Parameter optimization was performed using the genetic algorithm and by minimizing an objective score, the equation for which is given in Table S4. Two physicochemical constraints were applied to the model, i.e. solution electroneutrality and ion solubility. To ensure electroneutrality, the error was defined by the sum of the squared positive and negative charges in the cytoplasm and the vacuole relative to the total quantity of charges in the respective compartments (Table S4). The solubility product constant (K_{sp}), which is the result of the multiplication of the free ion concentrations according to their stoichiometry in the complex, must be smaller or equal to the K_{sp} of the given complex. The whole iterative process was then repeated by means of parallel computing, using the Curta cluster housed by the Mesocentre de Calcul Intensif Aquitain (MCIA). The 200 best-scoring parameter sets were kept for further analysis.

To evaluate the goodness of fit of the model, the relative root mean squared error (*RRMSE*) was calculated for each variable, giving the same weight for solution electroneutrality, ion complexation and tissue osmolality, according to the following equation (Wallach et al., 2014):

$$RRMSE = \sqrt{\frac{1}{42}\sum_{k=1}^{z}\sum_{c=1}^{7}\left(\frac{K_{sp,c,k}^{cal}-K_{sp,c,k}^{exp}}{K_{sp,c,k}^{exp}}\right)^2 + 7 \cdot \sum_{k=1}^{z}\left(\frac{Z_{cation}\cdot[free\ cations]_k + Z_{anion}\cdot[free\ anions]_k}{Z_{cation}\cdot[free\ cations]_k}\right)^z + 14 \cdot \left(\frac{Osm_{tissue}^{calc}-Osm_{tissue}^{Exp}}{Osm_{tissue}^{exp}}\right)^2},$$

where the subscript k stands for the subcellular compartment (vacuole or cytoplasm) in which the complexes and free ions are located, c stands for the seven ionic complexes, and calc and exp stand for modeled and experimental values, respectively. Note that the $K_{sp,c}^{exp}$ was not used as a constraint *per se* (i.e. $K_{sp,c}^{calc} \leq K_{sp,c}^{exp}$) during the optimization process, as the $K_{sp,c}^{exp}$ values were found to vary considerably in the literature (sometime with one order of magnitude) as a function of the temperature, ionic strength and viscosity of the bulk phase. Moreover, $K_{sp,c}^{exp}$ was assumed to be the same in both the vacuole and the cytoplasm (Table S5 and references hereafter).

Statistical analysis

Statistical analyses were carried out using R (R Core Team, Vienna, Austria, 2018). Normality and homogeneity of variance were analyzed by Levene tests. Comparisons of results from different conditions (treatment, age or both) were assessed using independent-samples Student's *t*-test, a one-way analysis of variance (ANOVA) followed by Duncan's test, or a two-way ANOVA, as described in the figure legends. Heat-map representations were obtained using the PHEATMAP package in R 1.0.12 after unidimensional hierarchical clustering by Pearson's correlation of mean-centered values of metabolites for different ages and treatments. To fit experimental data, parameters of non-linear regressions (logistic) were obtained using the non-linear least square function combined with Self-

Starting Nls Logistic Model (SSlogis) function, both from R-STAT 3.6.2. The coefficient of variation of simulated values was calculated as percentage between SD and mean values. To determine the accumulation rate, the derivatives of the time course of vacuolar ion concentrations were calculated from the cubic polynomial curve fit of the log-transformed data.

AUTHOR CONTRIBUTIONS

MDN and DM conceived and supervised the project. TP, MBGM, CC, YG, MDN and DM designed the experiments and analyzed the data. PP and AF performed the LC–MS analysis of fractionated samples. TP performed the experiments and set up the modeling, together with BB. TP, MDN, DM and BB wrote the article. All authors edited and approved the final version for publication.

CONFLICT OF INTEREST

The authors declare that they have no conflicts of interest associated with this work.

DATA AVAILABILITY STATEMENT

The data and scripts that support the findings of this study are openly available from the Institut National de la Recherche Agronomique (INRAE) (http://doi.org/10.15454/BL3GYM).

SUPPORTING INFORMATION

Additional Supporting Information may be found in the online version of this article.

Figure S1. Time course of shoot and root biomass of tomato plants.
Figure S2. Time-course of chlorophyll, total nitrogen, carbon, starch, and protein contents throughout the development of the fourth leaf.
Figure S3. Cytological analysis for volume determination.
Figure S4. Time course of main individual amino acids throughout the development of the fourth leaf.
Figure S5. Time course of main inorganic ions, organic acids and free sugars throughout the development of tomato leaf.

Figure S6. Time course of enzyme activities throughout the development of the fourth leaf of tomato.

Figure S7. Modeled vacuolar and cytoplasmic concentration of solutes throughout the development of the fourth leaf in tomato plants, without consideration of ion complexes within the vacuole and the cytoplasm.

Figure S8. Modeled vacuolar and cytoplasmic concentration of soluble solutes throughout the development of the fourth leaf in tomato plants, with consideration of ion complexes within the vacuole and the cytoplasm.

Figure S9. Comparison of subcellular concentrations of metabolites and ions estimated by model 1 with experimentally measured concentrations with NAF.

Figure S10. Comparison of subcellular concentrations of metabolites and ions estimated by model 2 with experimentally measured concentrations with NAF.

Figure S11. Comparison of subcellular concentrations of metabolites and ions estimated by model 3 with experimentally measured concentrations with NAF.

Figure S12. Coefficient of variation of simulated total concentrations and $\Delta\Psi$ as a function of leaf developmental stage.

Figure S13. Time course of vacuole expansion, accumulation and diffusion fluxes of individual solutes across tonoplast throughout the development of the fourth leaf of tomato plants.

Figure S14. Time course and curve fit of total vacuolar concentrations of ions and metabolites.

Figure S15. Time course of energy cost of solute transport and diffusion of individual solutes across the tonoplast throughout the development of the fourth leaf of tomato plants.

Figure S16. Impact of changing transporter mechanisms on modeled energy cost of vacuolar fluxes.

Figure S17. *In vivo* intracellular pH measurement in tomato leaf grown with ammonium and nitrate as the nitrogen source.

Table S1. Vacuolar and cytoplasmic proportion and concentration of main soluble metabolites and inorganic ions in 21-, 31- and 41-day-old leaves, determined by non-aqueous fractionation.

Table S2. Summary of transport mechanisms used for model parameterization.

Table S3. Parameterization of transport equations.

Table S4. Calculation of solution electroneutrality, osmolarity and objective score during parameter optimization.

Table S5. Constants used.

Table S6. Solubility product constants and permeability coefficients.

Table S7. Impact of changing transporter mechanism on goodness of fit.

Appendix S1. Modeling subcellular concentrations and calculation of ion transport rates across the tonoplast.

Appendix S2. Justification of the near-equilibrium hypothesis.

REFERENCES

Aarnes, H., Eriksen, A.B., Petersen, D. & Rise, F. (2007) Accumulation of ammonium in Norway spruce (*Picea abies*) seedlings measured by *in vivo* ^{14}N-NMR. *Journal of Experimental Botany*, **58**, 929–934.

Bai, L., Ma, X., Zhang, G., Song, S., Zhou, Y., Gao, L. *et al*.. (2014) A receptor-like kinase mediates ammonium homeostasis and is important for the polar growth of root hairs in Arabidopsis. *Plant Cell*, **26**, 1497–1511.

Baysdorfer, C. & Bassham, J.A. (1984) Spinach pyruvate kinase isoforms. *Plant Physiology*, **74**, 374–379.

Beauvoit, B.P., Colombié, S., Monier, A., Andrieu, M.H., Biais, B., Bénard, C. *et al*.. (2014) Model-assisted analysis of sugar metabolism throughout tomato fruit development reveals enzyme and carrier properties in relation to vacuole expansion. *Plant Cell*, **26**, 3224–3242.

Beshir, W.F., Tohge, T., Watanabe, M., Hertog, M.L.A.T.M., Hoefgen, R., Fernie, A.R. *et al*.. (2019) Non-aqueous fractionation revealed changing subcellular metabolite distribution during apple fruit development. *Horticulture Researc*, **6**, 98.

Biais, B., Bénard, C., Beauvoit, B., Colombié, S., Prodhomme, D., Ménard, G. *et al*.. (2014) Remarkable reproducibility of enzyme activity profiles in tomato fruits grown under contrasting environments provides a roadmap for studies of fruit metabolism. *Plant Physiology*, **164**, 1204–1221.

Brauer, D., Otto, J. & Tu, S.I. (1995) Selective accumulation of the fluorescent pH indicator, BCECF, in vacuoles of maize root-hair cells. *Journal of Plant Physiology*, **145**, 57–61.

Britto, D.T., Glass, A.D.M., Kronzucker, H.J. & Yaeesh Siddiqi, M. (2001) Cytosolic concentrations and transmembrane fluxes of NH_4^+/NH_3^- An evaluation of recent proposals. *Plant Physiology*, **125**, 523–526.

Britto, D.T. & Kronzucker, H.J. (2002) NH_4^+ toxicity in higher plants: a critical review. *Journal of Plant Physiology*, **159**, 567–584.

Britto, D.T. & Kronzucker, H.J. (2005) Nitrogen acquisition, PEP carboxylase, and cellular pH homeostasis: New views on old paradigms. *Plant, Cell and Environment*, **28**, 1396–1409.

Cruz, C., Domínguez-Valdivia, M.D., Aparicio-Tejo, P.M., Lamsfus, C., Bio, A., Martins-Loução, M.A. *et al*.. (2011) Intra-specific variation in pea responses to ammonium nutrition leads to different degrees of tolerance. *Environmental and Experimental Botany*, **70**, 233–243.

de la Peña, M., González-Moro, M.B. & Marino, D. (2019) Providing carbon skeletons to sustain amide synthesis in roots underlines the suitability of *Brachypodium distachyon* for the study of ammonium stress in cereals. *AoB Plants*, **11**, 1–11.

Destailleur, A., Cabasson, C., Alonso, A.P. *et al*.. (2021) The evolution of leaf function during development is reflected in profound changes in the metabolic composition of the vacuole. *Metabolites*, **11**, 848.

Estebana, R., Ariz, I., Cruz, C. & Moran, J.F. (2016) Mechanisms of ammonium toxicity and the quest for tolerance. *Plant Science*, **248**, 92–101.

Fricke, W. & Chaumont, F. (2005) Solute and water relations of growing plant cells. In: J.-P.V. & Vissenberg, K. (Eds.) *Plant Cell Monographs:The Expanding Cell*. Heidelberg: Springer Berlin, pp. 7–31.

Fürtauer, L., Weckwerth, W. & Nägele, T. (2016) A benchtop fractionation procedure for subcellular analysis of the plant metabolome. *Frontiers in Plant Science*, **7**, 1–14.

Gerendás, J. & Ratcliffe, R.G. (2000) Intracellular pH regulation in maize root tips exposed to ammonium at high external pH. *Journal of Experimental Botany*, **51**, 207–219.

Gibon, Y., Blaesing, O.E., Hannemann, J., Carillo, P., Ho, M., Palacios, N. *et al*.. (2004) A Robot-based platform to measure multiple enzyme activities in Arabidopsis using a set of cycling assays: comparison of changes of enzyme activities and transcript levels during diurnal cycles and in prolonged darkness. *Plant Cell*, **16**, 3304–3325.

Giglioli-Guivarc'h, N., Pierre, J.N., Vidal, J. & Brown, S. (1996) Flow cytometric analysis of cytosolic pH of mesophyll cell protoplasts from the crabgrass *Digitaria sanguinalis*. *Cytometry*, **23**, 241–249.

Hachiya, T., Inaba, J., Wakazaki, M., Sato, M., Toyooka, K., Miyagi, A. *et al*.. (2021) Glutamine synthetase causes ammonium toxicity in *Arabidopsis thaliana*. *Nature Communications*, **12**, 4944. Available at:. https://doi.org/10.1038/s41467-021-25238-7

Hachiya, T., Watanabe, C.K., Fujimoto, M., Ishikawa, T., Takahara, K., Kawai-Yamada, M. *et al*.. (2012) Nitrate addition alleviates ammonium toxicity without lessening ammonium accumulation, organic acid depletion and inorganic cation depletion in *Arabidopsis thaliana* shoots. *Plant & Cell Physiology*, **53**, 577–591.

Hase, T., Schürmann, P. & Knaff, D.B. (2006) The interaction of ferredoxin with ferredoxin-dependent enzymes. In: Golbeck, J.H. (Ed.) *Photosystem I: The Light-Driven Plastocyanin:Ferredoxin Oxidoreductase*. Dordrecht: Springer, pp. 477–498.

Hill, P.W., Raven, J.A. & Sutton, M.A. (2002) Leaf age-related differences in apoplastic NH_4^+ concentration, pH and the NH_3 compensation point for a wild perennial. *Journal of Experimental Botany*, **53**, 277–286.

Holtum, J.A.M. & Winter, K. (1982) Activity of enzymes of carbon metabolism during the induction of Crassulacean acid metabolism in *Mesembryanthemum crystallinum* L. *Planta*, **155**, 8–16.

Hoops, S., Gauges, R., Lee, C., Pahle, J., Simus, N., Singhal, M. *et al.*. (2006) COPASI - A COmplex PAthway SImulator. *Bioinformatics*, **22**, 3067–3074.

Kaiser, S., Eisele, S. & Scheuring, D. (2021) Vacuolar occupancy is crucial for cell elongation and growth regardless of the underlying mechanism. *Plant Signaling & Behavior*, **16**, e1922796.

Kaiser, S. & Scheuring, D. (2020) To lead or to follow: contribution of the plant vacuole to cell growth. *Frontiers in Plant Science*, **11**, 553.

Kirkby, E.A. & Mengel, K. (1967) Ionic balance in different tissues of the tomato plant in relation to nitrate, urea, or ammonium nutrition. *Plant Physiology*, **42**, 6–14.

Kronzucker, H.J., Siddiqi, M.Y. & Glass, A.D.M. (1997) Conifer root discrimination against soil nitrate and the ecology of forest succession. *Nature*, **385**, 59–61.

Krueger, S., Giavalisco, P., Krall, L., Steinhauser, M.C., Büssis, D., Usadel, B. *et al.*. (2011) A topological map of the compartmentalized *Arabidopsis thaliana* leaf metabolome. *PLoS One*, **6**, e17806.

Liu, Y., Lai, N., Gao, K., Chen, F., Yuan, L. & Mi, G. (2013) Ammonium inhibits primary root growth by reducing the length of meristem and elongation zone and decreasing elemental expansion rate in the root apex in *Arabidopsis thaliana*. *PLoS One*, **8**, e61031.

Liu, Y. & Von Wirén, N. (2017) Ammonium as a signal for physiological and morphological responses in plants. *Journal of Experimental Botany*, **68**, 2581–2592.

Lobit, P., Genard, M., Soing, P. & Habib, R. (2006) Modelling malic acid accumulation in fruits: Relationships with organic acids, potassium, and temperature. *Journal of Experimental Botany*, **57**, 1471–1483.

Loqué, D., Ludewig, U., Yuan, L. & Von Wirén, N. (2005) Tonoplast intrinsic proteins AtTIP2;1 and AtTIP2;3 facilitate NH$_3$ transport into the vacuole. *Plant Physiology*, **137**, 671–680.

Luna, E., Cassan, C., Prigent, S. & Chevanne, C. (2020) Metabolomics to exploit the primed immune system of tomato fruit. *Metabolites*, **10**, 1–19.

Martinière, A., Bassil, E., Jublanc, E., Alcon, C., Reguera, M., Sentenac, H. *et al.*. (2013) *In vivo* intracellular pH measurements in tobacco and arabidopsis reveal an unexpected pH gradient in the endomembrane system. *Plant Cell*, **25**, 4028–4043.

Meier, M., Liu, Y., Lay-Pruitt, K.S., Takahashi, H. & von Wirén, N. (2020) Auxin-mediated root branching is determined by the form of available nitrogen. *Nature Plants*, **6**, 1136–1145.

Nakata, P.A. (2012) Engineering calcium oxalate crystal formation in Arabidopsis. *Plant & Cell Physiology*, **53**, 1275–1282.

O'Leary, B.M., Rico, A., McCraw, S., Fones, H.N. & Preston, G.M. (2014) The infiltration-centrifugation technique for extraction of apoplastic fluid from plant leaves using *Phaseolus vulgaris* as an example. *Journal of Visualized Experiments*, **19**, 52113.

Ötvös, K., Marconi, M., Vega, A., O'Brien, J., Johnson, A., Abualia, R. *et al.*. (2021) Modulation of plant root growth by nitrogen source-defined regulation of polar auxin transport. *The EMBO Journal*, **40**, e106862.

Pasqualini, S., Ederli, L., Piccioni, C., Batini, P., Bellucci, M., Arcioni, S. *et al.*. (2001) Metabolic regulation and gene expression of root phosphoenolpyruvate carboxylase by different nitrogen sources. *Plant, Cell and Environment*, **24**, 439–447.

Podgórska, A., Burian, M., Gieczewska, K., Ostaszewska-Bugajska, M., Zebrowski, J., Solecka, D. *et al.*. (2017) Altered cell wall plasticity can restrict plant growth under ammonium nutrition. *Frontiers in Plant Science*, **8**, 1–19.

Podgórska, A., Gieczewska, K., Lukawska-Kuźma, K., Rasmusson, A.G., Gardeström, P. & Szal, B. (2013) Long-term ammonium nutrition of Arabidopsis increases the extrachloroplastic NAD(P)H/NAD(P)$^+$ ratio and mitochondrial reactive oxygen species level in leaves but does not impair photosynthetic capacity. *Plant, Cell and Environment*, **36**, 2034–2045.

Poucet, T., González-Moro, M.B., Cabasson, C., Beauvoit, B., Gibon, Y., Dieuaide-Noubhani, M. *et al.*. (2021) Ammonium supply induces differential metabolic adaptive responses in tomato according to leaf phenological stage. *Journal of Experimental Botany*, **72**, 3185–3199.

Raab, T.K. & Terry, N. (1995) Carbon, nitrogen, and nutrient interactions in *Beta vulgaris* L. as influenced by nitrogen source, NO3 versus NH4+. *Plant hysiology*, **107**, 575–584.

Rea, P.A. & Sanders, D. (1987) Tonoplast energization: Two H$^+$ pumps, one membrane. *Physiologia Plantarum*, **71**, 131–141.

Robert, G., Yagyu, M., Koizumi, T., Naya, L., Masclaux-Daubresse, C. & Yoshimoto, K. (2021) Ammonium stress increases microautophagic activity while impairing macroautophagic flux in Arabidopsis roots. *The Plant Journal*, **105**, 1083–1097.

Robert, G., Yagyu, M., Lascano, H.R., Masclaux-Daubresse, C. & Yoshimoto, K. (2021) A proposed role for endomembrane trafficking processes in regulating tonoplast content and vacuole dynamics under ammonium stress conditions in Arabidopsis root cells. *Plant Signaling & Behavior*, **16**, e1924977–e1924972.

Roberts, J.K.M. & Pang, M.K.L. (1992) Estimation of ammonium ion distribution between cytoplasm and vacuole using nuclear magnetic resonance spectroscopy. *Plant Physiology*, **100**, 1571–1574.

Roberts, J.K.M., Wemmer, D., Ray, P.M. & Jardetzky, O. (1982) Regulation of cytoplasmic and vacuolar pH in maize root tips under different experimental conditions. *Plant Physiology*, **69**, 1344–1347.

Sanchez-Zabala, J., González-Murua, C. & Marino, D. (2015) Mild ammonium stress increases chlorophyll content in *Arabidopsis thaliana*. *Plant Signaling & Behavior*, **10**, e991596.

Sarasketa, A., González-Moro, M.B., González-Murua, C. & Marino, D. (2014) Exploring ammonium tolerance in a large panel of *Arabidopsis thaliana* natural accessions. *Journal of Experimental Botany*, **65**, 6023–6033.

Sazzad Hossain, M., Persicke, M., Elsayed, A.I., Kalinowski, J. & Dietz, K.J. (2017) Metabolite profiling at the cellular and subcellular level reveals metabolites associated with salinity tolerance in sugar beet. *Journal of Experimental Botany*, **68**, 5961–5976.

Setién, I., Fuertes-Mendizabal, T., González, A., Aparicio-Tejo, P.M., González-Murua, C., González-Moro, M.B. *et al.*. (2013) High irradiance improves ammonium tolerance in wheat plants by increasing N assimilation. *Journal of Plant Physiology*, **170**, 758–771.

Stitt, M., Lilley, R.M., Richard, G. & Helot, H.W. (1989) Metabolite levels in specific cells and subcellular compartments of plant leaves. *Methods in Enzymology*, **174**, 518–552.

Swanson, S.J. & Jones, R.L. (1996) Gibberellic acid induces vacuolar acidification in Barley aleurone. *Plant Cell*, **8**, 2211–2221.

Van Beusichem, M.L., Kirkby, E.A. & Baas, R. (1988) Influence of nitrate and ammonium nutrition on the uptake, assimilation, and distribution of nutrients in *Ricinus communis*. *Plant Physiology*, **86**, 914–921.

Vega-mas, I., Cukier, C., Coleto, I., González-Murua, C., Limami, A.M., González-moro, M.B. *et al.*. (2019) Isotopic labelling reveals the efficient adaptation of wheat root TCA cycle flux modes to match carbon demand under ammonium nutrition. *Scientific Reports*, **9**, 925.

Vega-Mas, I., Pérez-Delgado, C.M., Marino, D., Fuertes-Mendizábal, T., González-Murua, C., Márquez, A.J. *et al.*. (2017) Elevated CO$_2$ induces root defensive mechanisms in tomato plants when dealing with ammonium toxicity. *Plant & Cell Physiology*, **58**, 2112–2125.

Volk, G.M., Lynch-Holm, V.J., Kostman, T.A., Goss, L.J. & Franceschi, V.R. (2002) The role of druse and raphide calcium oxalate crystals in tissue calcium regulation in *Pistia stratiotes* leaves. *Plant Biology*, **4**, 34–45.

Walch-Liu, P., Neumann, G., Bangerth, F. & Engels, C. (2000) Rapid effects of nitrogen form on leaf morphogenesis in tobacco. *Journal of Experimental Botany*, **51**, 227–237.

Wallach, D., Makowsk, D., Jones, J. & Brun, F. (2014) *Working with dynamic crop models: methods, tools and examples for agriculture and environment.* London: Elsevier B.V.

Wegner, L.H. & Shabala, S. (2019) Biochemical pH clamp: the forgotten resource in membrane bioenergetics. *The New Phytologist*, **225**, 37–47.

Wells, D.M. & Miller, A.J. (2000) Intracellular measurement of ammonium in *Chara corallina* using ion-selective microelectrodes. *Plant and Soil*, **221**, 103–106.